Gas Phase Hydrogenation of *m*-Dinitrobenzene over Alumina Supported Au and Au–Ni Alloy

Fernando Cárdenas-Lizana · Santiago Gómez-Quero · Mark A. Keane

Abstract We report, for the first time, 100% selectivity in the continuous gas phase hydrogenation of *m*-dinitrobenzene to *m*-nitroaniline (*m*-NAN) over Au/Al$_2$O$_3$. The synthesis and application of an alumina supported Au–Ni alloy is also described where alloy formation is demonstrated by XRD, diffuse reflectance UV–Vis and HRTEM analyses. Under the same reaction conditions, Au/Al$_2$O$_3$ delivered a higher (by close to an order of magnitude) hydrogenation rate compared with the alloy. Au–Ni/Al$_2$O$_3$ promoted the formation of both *m*-NAN and *m*-phenylenediamine, i.e. partial and complete hydrogenation: the results are consistent with a stepwise reduction mechanism.

Keywords Selective hydrogenation · *m*-dinitrobenzene · Au/Al$_2$O$_3$ · Au–Ni/Al$_2$O$_3$ · Supported alloy

1 Introduction

Aromatic amino compounds are important chemicals, used as intermediates in the manufacture of a range of fine chemicals, e.g. pesticides, pigments and cosmetics [1]. Amino derivates are typically synthesised via the reduction of the corresponding nitro-compound, either by Fe promoted reduction in acid media (Bechamp process) or transition metal promoted liquid phase hydrogenation [2]. The production of toxic by-products (ferric oxide sludge), in the former case, and the low associated target product yields has shifted attention to the catalytic hydrogenation option as a cleaner alternative [3]. Conventional supported monometallic (e.g. Pt or Pd) catalysts can deliver high conversions but an exclusive selectivity in terms of nitro-group reduction has yet to be achieved [4]. The ineffectiveness of these systems is particularly marked in the synthesis of *m*-nitroaniline (*m*-NAN) from *m*-dinitrobenzene (*m*-DNB) where the formation of *m*-phenylenediamine (*m*-PDM) (i.e. reduction of both –NO$_2$ groups) is also promoted [5, 6]. The use of Au in the selective hydrogenation of nitroarenes is now gaining increasing attention with recent reports of batch liquid phase hydrogenation over Au supported on SiO$_2$ [7], TiO$_2$ [8], Fe$_2$O$_3$ [8] and ZrO$_2$ [9] but the requirement of high hydrogen pressures (3–4 MPa) [7, 8] and/or the formation of highly toxic compounds (azoxy-derivates) [8, 9] represent decided drawbacks. Structure sensitivity has been proposed [10] while a selective activation of the nitro-group via interaction with Au sites may have a critical role to play [11]. We have recently reported reaction exclusivity in terms of –NO$_2$ group reduction for the continuous gas phase hydrogenation of a series of nitro-haloarenes over supported Au [12, 13]. We have now focused our attention on the selective hydrogenation of *m*-DNB and report here our preliminary results.

A significant recent development in catalysis by Au has seen the use of Au based alloys, which have delivered distinct selectivity and activity responses [14, 15]. Hutchings et al. [16], studying the gas phase hydrogenation of O$_2$ to H$_2$O$_2$, recorded higher activity (by a factor of 2) over a supported Au–Pd alloy when compared with Au and Pd. Pârvulescu et al. [17], using silica supported Au, Pd and Au–Pd in the hydrogenation of cinnamaldehyde, demonstrated that the alloy outperformed the monometallic catalysts in terms of activity and selectivity with respect to

F. Cárdenas-Lizana · S. Gómez-Quero · M. A. Keane (✉)
Chemical Engineering, School of Engineering and Physical Sciences, Heriot-Watt University, Edinburgh EH14 4AS, Scotland, UK
e-mail: M.A.Keane@hw.ac.uk

cinnamyl alcohol. Fierro et al. [18], in the gas phase hydrogenation of naphthalene over silica supported Au and Pt–Au, ascribed the higher activity observed for the bimetallic catalysts to the formation of a Pt–Au alloy. There is, however, a dearth of literature dealing with the catalytic implications of Ni–Au combinations and a comprehensive search did not unearth any study dealing with the preparation and catalytic application of an alumina supported Au–Ni alloy. Nevertheless, we can flag related studies involving supported Au–Ni systems: (i) Molenbroek et al. [19] reported improved butane steam reforming stability for reaction over Au–Ni/SiO$_2$ relative to Ni/SiO$_2$ and ascribed this response to the formation of a Au–Ni surface alloy that served to limit coke deposition and prolong catalytic activity; (ii) Triantafyllopoulos and Neophytides [20] and Chin et al. [21] have noted that the addition of Au to Ni/YSZ and Ni/MgAl$_2$O$_4$ served to suppress carbon deposition during methane steam reforming; (iii) Yuan et al. [22] observed an enhanced hydrodechlorination activity over Au–Ni/SiO$_2$ and Au–Ni/TiO$_2$ that they associated with a surface Au–Ni synergism.

In this paper we provide the first report of the catalytic action of Au/Al$_2$O$_3$ in the gas phase hydrogenation of *m*-DNB, comparing activity/selectivity with that obtained using an Al$_2$O$_3$ supported Au–Ni alloy. We link catalyst performance to critical structural information.

2 Experimental

2.1 Catalyst Preparation and Activation

The Al$_2$O$_3$ support (Puralox) was obtained from Condea Vista Co. and used as received. A 1 mol % Au/Al$_2$O$_3$ sample was prepared by impregnation with HAuCl$_4$ (Aldrich, 0.0025 g cm^{-3}). The slurry was heated (ca. 2 K min^{-1}) to 353 K and maintained under agitation (600 rpm) with a constant He purge. The solid residue was dried in a flow of He at 383 K for 5 h. A Ni/Al$_2$O$_3$ (10 mol %) was prepared by impregnation where a 2-butanolic Ni(NO$_3$)$_2$ solution was added drop wise at 353 K to the substrate with constant agitation (600 rpm) and oven dried at 393 K for 12 h. The alumina supported Au–Ni precursor was prepared by activation of the Ni/Al$_2$O$_3$ catalyst in a stream of H$_2$ at 2 K min^{-1} to 723 ± 1 K, which was maintained for 2.5 h. The gas flow was switched to He and cooled to room temperature, at which point the sample was passivated in 1% v/v O$_2$/He. This treatment served to provide a protective oxide layer over the surface Ni that prevented bulk oxidation upon exposure to the atmosphere. The passivated sample was contacted with HAuCl$_4$, posttreatment as above. After preparation, the sample (sieved into a batch of 75 μm average diameter) was activated in 60 cm^3 min^{-1} H$_2$ at 2 K min^{-1} to 603 ± 1 K, cooled to room temperature in a He flow and subsequently subjected to a temperature controlled treatment in 65 cm^3 min^{-1} N$_2$ at 50 K min^{-1} to 1273 ± 1 K. The latter step was necessary to generate the supported alloy as the Au–Ni miscibility gap is such that bulk alloy formation is not possible at temperatures below 1083 K [23]. The Au/Al$_2$O$_3$ sample underwent the same annealing treatment to facilitate a direct comparison of catalytic performance with that of the alloy. The samples were then cooled in N$_2$ and passivated in 1% v/v O$_2$/He at room temperature for offline analysis. Metal loading was determined (to within ±2%) by inductively coupled plasma-optical emission spectrometry (ICP-OES, Vista-PRO, Varian Inc.) from the diluted extract of aqua regia.

2.2 Catalyst Characterization

Temperature programmed reduction (TPR) and H$_2$ chemisorption were determined using the commercial CHEM-BET 3000 (Quantachrome) unit. The samples were loaded into a U-shaped Quartz cell (100 mm × 3.76 mm i.d.) and heated in 17 cm^3 min^{-1} 5% v/v H$_2$/N$_2$ (Brooks mass flow controlled) to 603 ± 1 K (Au/Al$_2$O$_3$ and Au–Ni/Al$_2$O$_3$) or 723 ± 1 K (Ni/Al$_2$O$_3$) at 2 K min^{-1}. The effluent gas passed through a liquid N$_2$ trap and H$_2$ consumption was monitored by a thermal conductivity detector, with data acquisition/manipulation using the TPR Win^{TM} software. The reduced samples were maintained at the final temperature until the signal returned to the baseline. After the reduction step, the catalysts were cooled in a He flow and subjected to the annealing step described above, with subsequent H$_2$ chemisorption (at room temperature) using a pulse (10 μl) titration procedure, as described elsewhere [24]. BET surface area analysis and total pore volume were performed using the commercial Micromeritics Flowsorb II 2300 unit. Prior to analysis, the samples were outgassed at 423 K for 1 h in 20 cm^3 min^{-1} N$_2$. BET area was obtained in a 30% v/v N$_2$/He flow (20 cm^3 min^{-1}) with at least three cycles of N$_2$ adsorption–desorption using the standard single-point BET method. Total pore volume was obtained at a relative N$_2$ pressure of $P/P_0 = 0.95$. The BET area and pore volume data were reproducible to within ±3% and the values quoted in this paper are the mean. Powder X-ray diffractograms were recorded on a Bruker/Siemens D500 incident X-ray diffractometer using Cu Kα radiation. The samples were scanned at 0.02° step^{-1} over 20° ≤ 2θ ≤ 90° (scan time = 5 s step^{-1}). Diffractograms were identified using the JCPDS-ICDD reference standards, i.e. γ-Al$_2$O$_3$ (10-0425), Au (4-0784) and Ni (45-1027), and Ref. [25] for the Au–Ni alloy. Metal particle size (d_{hkl}) was estimated using the Scherrer equation:

$$d_{hkl} = \frac{K \cdot \lambda}{\beta \cdot \cos \theta} \tag{1}$$

where $K = 0.9$, λ is the incident radiation wavelength (1.54056 Å), β is the peak width at half the maximum intensity and θ represents the diffraction angle corresponding to the main plane associated with metallic Au ($2\theta = 38.1°$) and Au–Ni alloy ($2\theta = 42.8°$). Diffuse reflectance UV–Vis (DRS UV–Vis) measurements were conducted using a Perkin Elmer Lambda 35 UV–Vis Spectrometer with $BaSO_4$ powder as reference; absorption profiles were calculated from the reflectance data using the Kubelka–Munk function. Transmission electron microscopy analysis was conducted using a JEOL JEM 2011 HRTEM unit with a UTW energy dispersive X-ray detector (Oxford Instruments) operated at an accelerating voltage of 200 kV, employing Gatan DigitalMicrograph 3.4 for data acquisition/manipulation. The specimens were prepared by dispersion in acetone and deposited on a holey carbon/Cu grid (300 Mesh).

2.3 Catalysis Procedure

Reactions were carried out under atmospheric pressure, in situ immediately after activation, in a fixed bed vertical plug-flow glass reactor (l = 600 mm; i.d. =15 mm) at 573 K. The catalytic reactor and operating conditions to ensure negligible heat/mass transport limitations have been fully described elsewhere [26]. Isothermal reaction conditions (± 1 K) were ensured by diluting the catalyst bed with ground glass (75 μm). The reaction temperature was continuously monitored by a thermocouple inserted in a thermowell within the catalyst bed. A butanolic solution of *m*-DNB was delivered to the reactor via a glass/teflon airtight syringe and teflon line using a microprocessor controlled infusion pump (Model 100 kd Scientific) at a fixed calibrated flow rate. A co-current flow of *m*-DNB and ultra pure H_2 (<1% v/v *m*-DNB/H_2) was maintained at $GHSV = 2 \times 10^4$ h^{-1} with a molar metal (n) to inlet molar –NO_2 feed rate (F) ratio that spanned the range 15–50×10^{-3} h; inlet *m*-DNB flow = 0.05–0.15 mmol h^{-1}. The H_2 content was up to 300 times in excess of the stoichiometric requirement, the flow rate of which was monitored using a Humonics (Model 520) digital flowmeter. In a series of blank tests, passage of *m*-DNB in a stream of H_2 through the empty reactor or over the support alone, i.e. in the absence of Au or Au–Ni, did not result in any detectable conversion. The reactor effluent was frozen in a liquid N_2 trap for subsequent analysis which was made using a Perkin-Elmer Auto System XL gas chromatograph equipped with a programmed split/splitless injector and a flame ionization detector, employing a DB-1 50 m × 0.20 mm i.d., 0.33 μm film thickness capillary column

(J&W Scientific). *m*-DNB (Aldrich, ≥ % purity) and the solvent (1-butanol: Riedel-de Haën) were used as supplied without further purification. The degree of nitro-group reduction (x_{-NO_2}) is given by

$$x_{-NO_2} = \frac{[-NH_2]_{out}}{[-NO_2]_{in}} = \frac{2 \times [m-PDM]_{out} + [m-NAN]_{out}}{2 \times [m\text{-DNB}]_{in}} \tag{2}$$

where [*m*-NAN] and [*m*-PDM] are, respectively, the concentrations of *m*-NAN and *m*-PDM and the subscripts *in* and *out* refer to the inlet and outlet streams. Catalyst activity is also quantified in terms of the fractional conversion of *m*-DNB ($x_{m\text{-}DNB}$)

$$x_{m-DNB} = \frac{[m-DNB]_{in} - [m-DNB]_{out}}{[m\text{-DNB}]_{in}} \tag{3}$$

while selectivity in terms of (say) *m*-NAN ($S_{m\text{-NAN}}$) is given by

$$S_{m-NAN} = \frac{[m-NAN]_{out}}{[m\text{-DNB}]_{in} - [m\text{-DNB}]_{out}} \tag{4}$$

Repeated reactions using different samples from the same batch of catalyst delivered conversion/selectivity data that were reproducibility to within $\pm 6\%$.

3 Result and Discussion

Characterisation measurements are presented in Table 1, which include the T_{max} values associated with the TPR of the catalyst precursors and critical values (H_2 uptake, BET

Table 1 Temperature programmed reduction (TPR) T_{max} values, H_2 uptake, BET surface areas, total pore volumes, metal particle size and DRS UV-Vis spectroscopic characteristics for Au/Al$_2$O$_3$ and Au-Ni/Al$_2$O$_3$ with associated pseudo-first order rate constants (k) and reaction products (+selectivities) obtained under conditions of equal activity ($x_{m\text{-DNB}} \sim 0.15$) in the reduction of *m*-DNB

	Au/Al$_2$O$_3$	Au–Ni/Al$_2$O$_3$
TPR T_{max} (K)[a]	**434**	446, **603**
H_2 uptake (μmol g$_{catalyst}^{-1}$)	0.1	0.2
BET area (m^2 g^{-1})	122	68
Pore Volume (10^{-3} cm^3 g^{-1})	258	212
d_{hkl} (nm)[b]	37	23[c]
DRS UV–Vis A_{max} (nm)	540	–[d]
k (10^3 $mmol_{-NO_2}$ mol_{metal}^{-1} h^{-1})	2.0	0.3
Product(s) (% selectivity)	*m*-NAN (100)	*m*-NAN (75)
		m-PDM (25)

[a] T_{max} associated with the dominant TPR peak is given in bold

[b] Based on XRD line broadening analysis: see Eq. 1

[c] Based on XRD response at $2\theta = 42.8°$

[d] No distinguishable peak(s)

surface area, pore volume, average metal particle size and characteristic DRS UV–Vis absorbance peaks) associated with the activated catalysts. The catalytic properties of the two systems were evaluated using the gas phase hydrogenation of *m*-DNB as a model reaction. Conversion of *m*-DNB generated *m*-NAN (partial nitro-group reduction) and *m*-PDM (complete nitro-group reduction) as the sole products with no evidence of hydrodenitrogenation or aromatic ring reduction.

3.1 Au/Al₂O₃

3.1.1 Catalyst Characterization

The result of the TPR analysis for Au/Al₂O₃ is presented in Fig. 1 (profile I) where the appearance of a single positive peak (T = 434 K) can be attributed to the reduction of Au^{3+} to Au^0, as proposed elsewhere [27]. Bus et al. [28], using time-resolved in situ XAS, have established the presence of Al₂O₃-supported oxidic or hydroxidic Au^{3+} species in the precursor that were reduced in H₂ at 440 K to yield metallic Au. Hydrogen uptake (Table 1) on the activated sample was low, consistent with the limited H₂ chemisorptive capacity of supported gold reported in the literature [10]. The X-ray diffraction pattern for Au/Al₂O₃ is given in Fig. 2 (profile Ia) with four broad peaks between 30° and 70°, corresponding to the (311), (222), (400) and (440) planes associated with cubic γ-Al₂O₃ (JCPDS-ICDD 10-0425). In addition, the peaks at 2θ = 38.1°, 44.4°, 64.7° and 77.5° consistent with, respectively, the (111), (200),
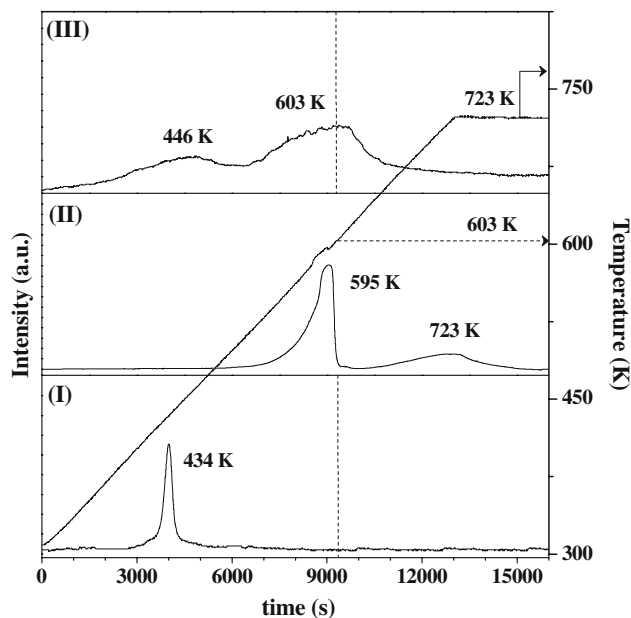

Fig. 1 TPR profiles for **(I)** Au/Al₂O₃, **(II)** Ni/Al₂O₃ and **(III)** Au–Ni/Al₂O₃. Dashed line represents final isothermal hold for Au/Al₂O₃ and Au–Ni/Al₂O₃
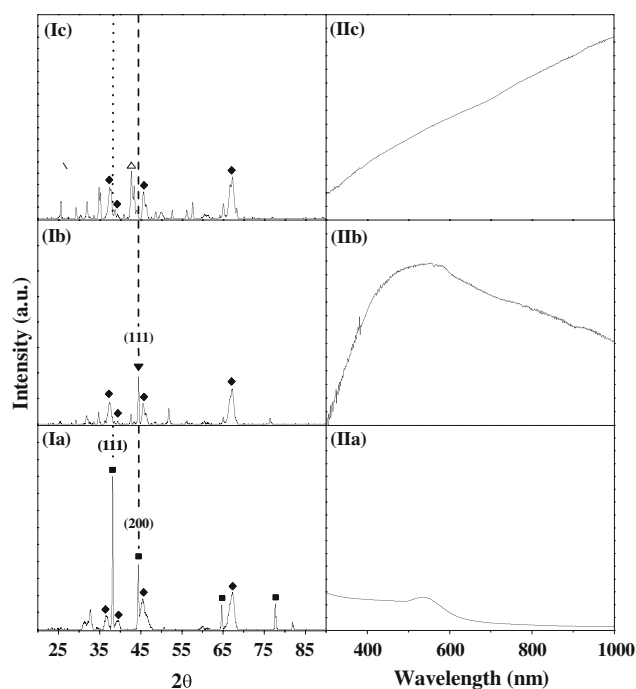

Fig. 2 **(I)** XRD patterns and **(II)** DRS UV–Vis spectra for **(a)** Au/Al₂O₃, **(b)** Ni/Al₂O₃ and **(c)** Au–Ni/Al₂O₃. *Note*: Dotted line identifies position of the (111)$_{Au}$ peak and dashed line the position of the (200)$_{Au}$ and (111)$_{Ni}$ peaks. JCPDS-ICDD reference data: (◆) γ-Al₂O₃ (10-0425); (■) Au (4-0784), (▼) Ni (45-1027) and (Δ) Au–Ni alloy [25]

(220) and (311) planes of metallic Au (JCPDS-ICDD 4-0784). The DRS UV–Vis spectrum for Au/Al₂O₃ (Fig. 2, profile IIa) presents a maximum at 540 nm corresponding to metallic Au, where the weak signal intensity is due to the low Au loading in the sample. Gluhoi et al. [29] have ascribed a DRS UV–Vis band between 500–600 nm, for Au/Al₂O₃ prepared by deposition–precipitation, to the presence of Au^0. Representative TEM images are presented in Fig. 3. In common with reported TEM analyses of impregnated Au/Al₂O₃ [12, 13, 30], the Au is present as discrete particles with a pseudo-spherical morphology. The Au particles present a wide size distribution (<5–200 nm). Selected area electron diffraction analysis confirmed that Au was present in the metallic form.

3.1.2 Catalyst Activity/selectivity

In the conversion of *m*-DNB, Au/Al₂O₃ delivered 100% selectivity to the partially reduced *m*-NAN. This product is a valuable raw material employed in the manufacture of several fine chemicals [1]. Reactant conversion, presented in Fig. 4(I) as the ratio of *m*-DNB in the exit ($(n)_{out}$) relative to that in the inlet ($(n)_{in}$) stream, exhibited essentially a temporal invariance. We have already established [12, 13] the applicability of a pseudo-first order kinetic treatment for nitoarene reduction over supported Au where
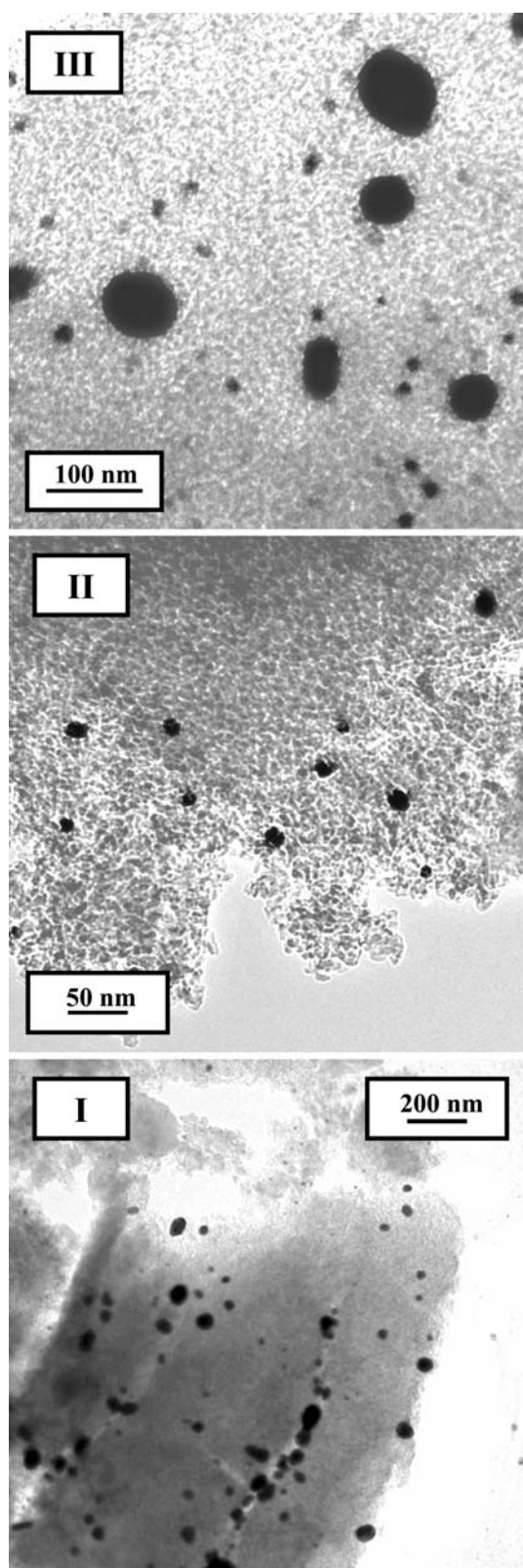
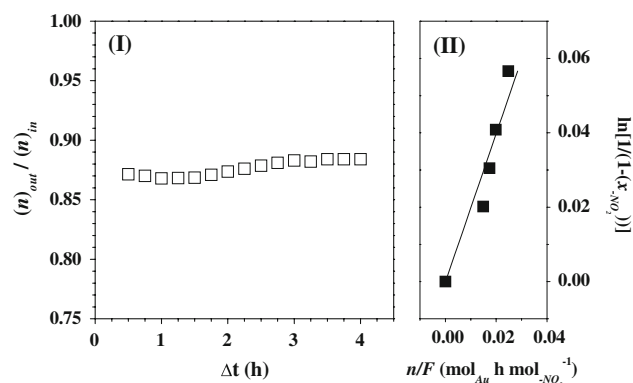**Fig. 3** Representative TEM images of Au/Al$_2$O$_3$; (**I**) low, (**II**) and (**III**) medium resolution

Fig. 4 (**I**) Ratio of *m*-DNB in the exit stream $((n)_{\text{out}})$ relative to that in the inlet stream $((n)_{\text{in}})$ for reaction $(-NO_2/Au = 40$ $mol_{-NO_2} \, mol_{Au}^{-1} \, h^{-1})$ over Au/Al$_2$O$_3$; (**II**) Pseudo-first-order kinetic plot for the reduction of *m*-DNB

$$\ln\left[\frac{1}{(1 - (x_{-\mathrm{NO_2}}))}\right] = \mathrm{k}\left(\frac{n}{F}\right) \tag{5}$$

The parameter $(x_{-\mathrm{NO_2}})$ represents hydrogenation activity and (n/F) has the physical meaning of contact time. The linear relationship between $\ln((1 - (x_{-\mathrm{NO_2}}))^{-1})$ and n/F is shown in Fig. 4(II) and the resultant pseudo-first order rate constant (k) is given in Table 1. The available published data dealing with the selective hydrogenation of *m*-DNB are very limited and we could not find any report that has demonstrated the exclusive formation of *m*-NAN. It is, nevertheless, worth flagging work conducted at high hydrogen pressures (10–45 atm) in the gas phase over Pt/C under supercritical CO$_2$ ($P_{\mathrm{CO_2}} = 150 \, atm$) [31] and in the liquid phase using Pd/C [32] and polylvinylpyrrolidone stabilized Ru/Al$_2$O$_3$ [33] where *m*-NAN selectivities in excess of 80% have been recorded.

3.2 Au–Ni/Al$_2$O$_3$

3.2.1 Catalyst Characterization

The TPR response (Fig. 1, profile II) for the Ni/Al$_2$O$_3$ precursor is characterised by two stages of reduction during the temperature ramp with peak maxima at 595 K and 723 K, corresponding to the sequential Ni(NO$_3$)$_2$ → NiO → Ni^0 steps [24]. TPR of Au–Ni/Al$_2$O$_3$ (see profile III), prepared by the reductive deposition of Au onto passivated Ni, was accompanied by a low intensity H$_2$ consumption response with two ill-defined peaks at 446 and 603 K. In this preparative route (direct redox method), Ni with a lower electrochemical potential serves to reduce the deposited Au precursor (HAuCl$_4$) and, consequently, undergoes oxidation [34]. In common with Au/Al$_2$O$_3$,

Au–Ni/Al$_2$O$_3$ also exhibited a low H$_2$ uptake (<1 μmol g^{-1}). BET area of both supported catalysts was significantly lower than that of the starting Al$_2$O$_3$ support (190 m^2 g^{-1}). This decrease in area was accompanied by a reduction in pore volume (Table 1), which can be attributed to a partial pore filling by the metal particles.

XRD analysis was undertaken to demonstrate Au–Ni alloy formation (see Fig. 2). The diffractogram generated for Ni/Al$_2$O$_3$ (profile Ib) is characterised by a peak at $2\theta = 44.5°$ due to the (111) plane of metallic Ni (JCPDS-ICDD 45-1027). XRD analysis of the bimetallic sample (profile Ic) did not reveal any peaks due to the individual metals (Au or Ni) but a new metallic phase is in evidence, with a characteristic $2\theta = 42.8°$, that is located between the peaks for (111)$_{Au}$ ($2\theta = 38.1°$) and (111)$_{Ni}$ ($2\theta = 44.5°$), the positions of which are illustrated in Fig. 2 by dotted and dashed vertical lines, respectively. This new phase can be attributed to the formation of a Au–Ni alloy. Indeed, this assertion is supported by the work of Togasaki et al. [25] who attributed an XRD peak at $2\theta = 42°$ to amorphous

Au–Ni alloy (8–51% mol Au) prepared by the addition of KAu(CN)$_2$ to a Ni–W plating bath. Metal particle size was evaluated by the standard Scherrer line broadening approach (Table 1) where the metal particle size was smaller in the alloy compared with the monometallic sample. Au–Ni alloy formation is also supported by DRS UV–Vis analysis. The DRS UV–Vis response for Ni/Al$_2$O$_3$ shows a maximum (530–580 nm) that corresponds to metallic Ni [35]. In marked contrast, the spectrum recorded for Au–Ni/Al$_2$O$_3$ (profile IIc) did not generate any detectable peak/signal corresponding to metallic Au or Ni. Indeed, Mulvaney [36] established the formation of a Au–Ag alloy on the basis that the DRS UV–Vis spectrum did not exhibit the absorption bands for the component metals. Representative low (I), medium (II and III) and high (IV) resolution TEM images of Au–Ni/Al$_2$O$_3$ are presented in Fig. 5. The particles exhibit a predominantly pseudo-spherical morphology, with a wide size distribution (<5–200 nm), similar to that observed for Au/Al$_2$O$_3$. The diffractogram pattern for an isolated particle is shown in Fig. 5(IV) where the characteristic

Fig. 5 Representative TEM images of Au–Ni/Al$_2$O$_3$; (I) low, (II) and (III) medium and (IV) high resolution
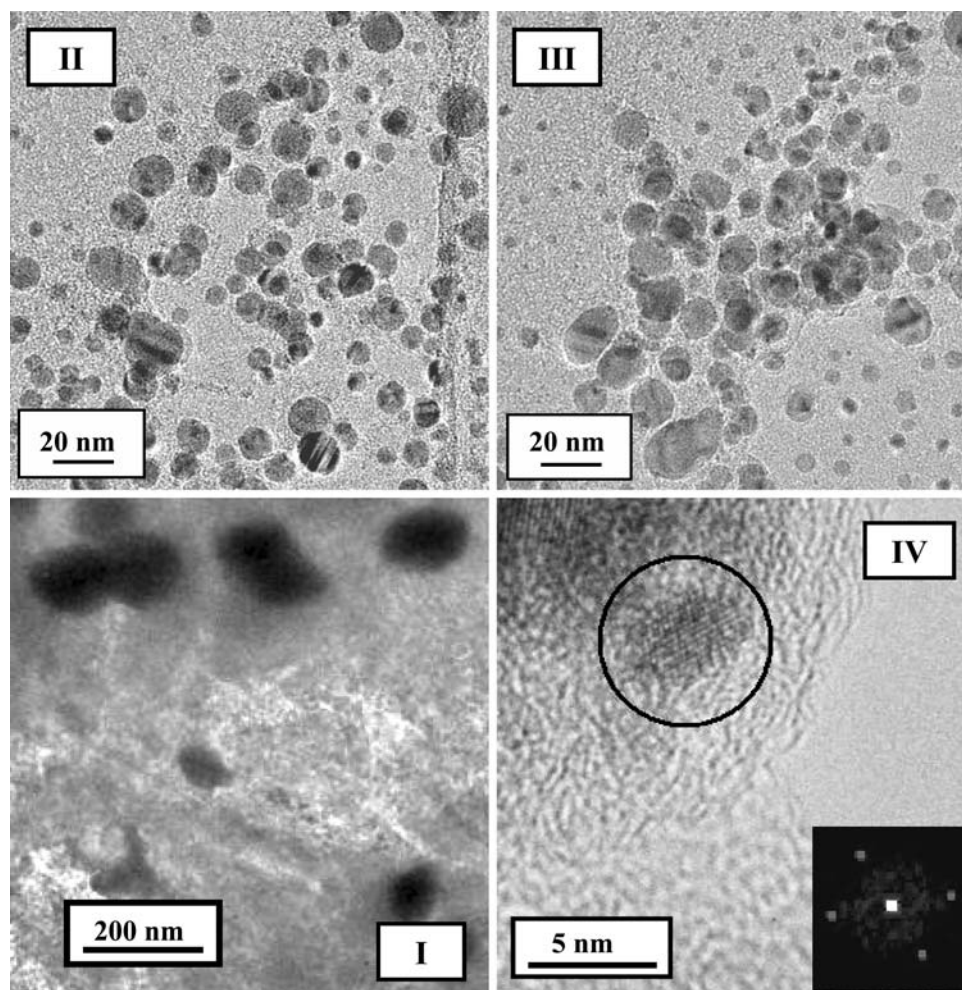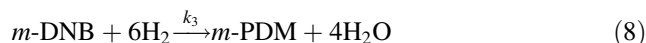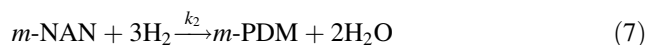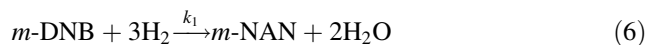
d-spacing is consistent with that obtained by XRD, confirming alloy formation.

3.2.2 Catalyst Activity/Selectivity

A pseudo-first order kinetic treatment of the data generated for Au–Ni/Al$_2$O$_3$ is presented in Fig. 6(I) and the associated rate constant value (k) is given in Table 1. The studies to date that have considered Au based alloy systems (Au–Pd [17, 37] and Au–Pt [18]) have resulted in an increased hydrogenation activity relative to the monometallic Au catalyst. In this study Au–Ni/Al$_2$O$_3$ delivered a significantly lower (by a factor of 7) rate compared with Au/Al$_2$O$_3$. We could not find any directly related study that has compared the hydrogenation performance of a supported Au–Ni alloy with that of the constituent metals. Chin et al. [21] employed MgAl$_2$O$_4$-supported Au–Ni alloy to promote CH$_4$ reforming and observed a decrease in catalytic activity that was ascribed to an occlusion of the Ni step and edge sites by Au. Vasil'kov et al. [38] have recently quoted an increased catalytic activity (up to two orders of magnitude) for the isomerization of allylbenzene over Au–Ni/SiO$_2$ as a consequence of a surface Au–Ni synergism (demonstrated by XPS). A series of experiments were conducted to probe the effect(s) of alloy formation on reaction selectivity. The results are presented in Fig. 6(II) where quite distinct selectivity responses are in evidence. While Au/Al$_2$O$_3$ delivered 100% selectivity to the partially

Fig. 6 (**I**) Pseudo-first-order kinetic plot for the reduction of *m*-DNB over Au–Ni/Al$_2$O$_3$; (**II**) Variation of *m*-PDM (solid symbols) and *m*-NAN (open symbols) selectivity (*S*) with *m*-DNB fractional conversion (x_{m-DNB}) for reaction over Au/Al$_2$O$_3$ (■/□, solid line) and Au–Ni/Al$_2$O$_3$ (▲/△, dashed line); (**III**) Dependence of *m*-NAN mole fraction (N_{m-NAN}) on *m*-DNB conversion for reaction over Au–Ni/Al$_2$O$_3$. Note: line represents fit to the parallel/consecutive model, see Eq. 14

reduced *m*-NAN, Au–Ni/Al$_2$O$_3$ generated a mixture of partially and fully (*m*-PDM) reduced products with a shift in favour of the latter with increasing *m*-DNB conversion. We tentatively link the differences in the activity/selectivity responses presented in Fig. 6(II) for the two systems to differences in reactant adsorption/activation. Indeed, a distinct mechanism for the adsorption of nitroarenes on Au compared with Au–M (*M* = Pb, Tl) has been proposed elsewhere [39]. The hydrogenation of *m*-DNB can proceed via consecutive/parallel steps according to:

$$m\text{-DNB} + 3H_2 \xrightarrow{k_1} m\text{-NAN} + 2H_2O \qquad (6)$$

$$m\text{-NAN} + 3H_2 \xrightarrow{k_2} m\text{-PDM} + 2H_2O \qquad (7)$$

$$m\text{-DNB} + 6H_2 \xrightarrow{k_3} m\text{-PDM} + 4H_2O \qquad (8)$$

and

$$\frac{dN_{m-DNB}}{d(n/F_{m-DNB})} = -(k_1 + k_3) \times N_{m-DNB} \qquad (9)$$

$$\frac{dN_{m-NAN}}{d(n/F_{m-DNB})} = k_1 \times N_{m-DNB} - k_2 \times N_{m-NAN} \qquad (10)$$

$$\frac{dN_{m-PDM}}{d(n/F_{m-DNB})} = k_2 \times N_{m-NAN} + k_3 \times N_{m-DNB} \qquad (11)$$

where N_i represents the molar fraction of the ith compound and k_j is the pseudo-first order rate constant of step *j*. Combination of Eqs. 9 and 10 gives

$$\frac{dN_{m-NAN}}{dN_{m-DNB}} = -L + M \times \left(\frac{N_{m-NAN}}{N_{m-DNB}} \right) \qquad (12)$$

with

$$L = \frac{k_1}{k_1 + k_3} \quad \therefore \quad M = \frac{k_2}{k_1 + k_3} \qquad (13)$$

which, by formal integration, results in:

$$N_{m-NAN} = \frac{L}{1 - M} \times \left(N_{m-DBN}^M - N_{m-DBN} \right) \qquad (14)$$

The values of *L* and *M* determine the preferred reaction pathway; a stepwise –NO$_2$ group reduction mechanism (with *m*-NAN as intermediate) should result in a value for *L* close to unity ($k_3 \sim 0$) and $M > 1$ ($k_2 > (k_1 + k_3)$). Indeed, the fit of our experimental results for Au–Ni/Al$_2$O$_3$ to Eq. 14 (see Fig. 6III) yields values of $L = 1.1$ and $M = 5.0$ that are consistent with a stepwise reaction network.

One unique aspect of this work has been the exclusive production of the partially reduced *m*-NAN product over Au/Al$_2$O$_3$, i.e. ($k_1 \gg (k_2 + k_3)$). This level of exclusivity in a continuous process can serve as the basis for the development of a new sustainable route to a range of high value amino-compounds. Moreover, we have provided the
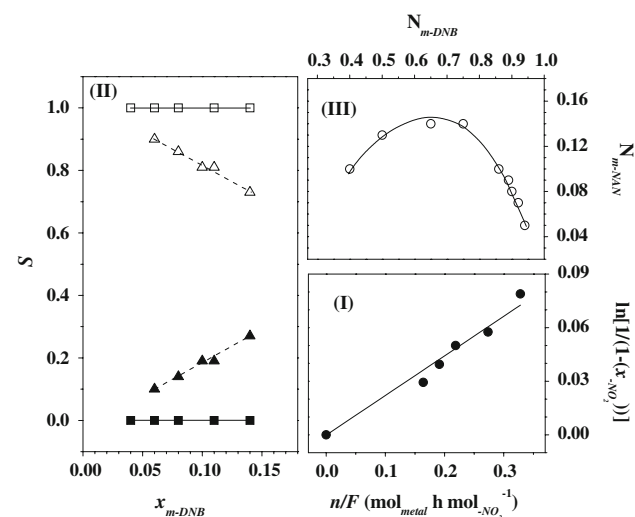
first reported catalytic application of (alumina) supported Au–Ni alloy in a hydrogenation process. The requirement of a high treatment temperature to form the supported alloy [23] (see Sect. 2), which was also applied to Au/Al$_2$O$_3$ to facilitate a direct comparison of catalytic performance, has resulted in the formation of larger supported metal particles (see Table 1, Figs. 3 and 5). The dependence of activity and selectivity on particle size in Au catalytic systems is still unclear. It has been proposed that surface defects and smaller Au particle sizes (<10 nm) are required for significant hydrogenation activity [10]. Bailie et al. [40], studying the hydrogenation of but-2-enal over Au/ZnO, have suggested that a high selectivity to but-2-en-1-ol required larger Au particles (10–20 nm). Moreover, Hofmeister et al. [41] reported lower hydrogenation rates associated with Au particles <2 nm and ascribed this to quantum size effects that modified the electronic properties of the Au particles. Future work will focus on the role of particle size in selective hydrogenation with a consideration of alternative catalyst formulations, activation and reaction conditions with the goal of delivering enhanced reaction rates while retaining the product exclusivity that we report here.

4 Conclusions

The results presented in this report demonstrate that Au/Al$_2$O$_3$ exclusively promotes the partial reduction of m-DNB to m-NAN in gas phase continuous operation with no detectable catalyst deactivation (up to 4 h on-stream). We have provided, for the first time, evidence of catalytic hydrogenation activity associated with an alumina supported Au–Ni alloy. Alloy formation has been established by XRD (new reflection at $2\theta = 42.8°$) and confirmed by TEM analyses. In addition, the DRS UV–Vis spectrum for Au-Ni/Al$_2$O$_3$ did not exhibit the absorption bands that characterised Au/Al$_2$O$_3$ and Ni/Al$_2$O$_3$. The supported alloy delivered a lower hydrogenation rate (by almost an order of magnitude) and promoted both partial and complete hydrogenation, following a stepwise reaction mechanism.

References

1. Vogt PF, Gerulis JJ (2005) Ullmann's encyclopedia of industrial chemistry. Aromatic amines. Wiley-VCH Verlag GmbH & Co. KGaA, Weinheim
2. Wang XD, Liang MH, Zhang JL, Wang Y (2007) Curr Org Chem 11:299
3. Westerterp KR, Molga EJ, van Gelder KB (1997) Chem Eng Process 36:17
4. Vishwanathan V, Jayasri V, Basha PM, Mahata N, Sikhwivhilu LM, Coville NJ (2008) Catal Commun 9:453
5. Liu YX, Chen JX, Zhang JY (2007) Chin J Chem Eng 15:63
6. Telkar MM, Nadgeri JM, Rode CV, Chaudhari RV (2005) Appl Catal A Gen 295:23
7. Chen Y, Qiu J, Wang X, Xiu J (2006) J Catal 242:227
8. Corma A, Serna P (2006) Science 313:332
9. He D, Shi H, Wu Y, Xu B-Q (2007) Green Chem 9:849
10. Claus P (2005) Appl Catal A Gen 291:222
11. Boronat M, Concepción P, Corma A, González S, Illas F, Serna P (2007) J Am Chem Soc 129:16230
12. Cárdenas-Lizana F, Gómez-Quero S, Keane MA (2008) ChemSusChem 1:215
13. Cárdenas-Lizana F, Gómez-Quero S, Keane MA (2008) Catal Commun 9:475
14. Joseph T, Kumar KV, Ramaswamy AV, Halligudi SB (2007) Catal Commun 8:629
15. Hutchings GJ (2008) Chem Commun 1148
16. Edwards JK, Carsley AF, Herzing AA, Kiely CJ, Hutchings GJ (2008) Faraday Discuss 138:225
17. Pârvulescu VI, Pârvulescu V, Endruschat U, Filoti G, Wagner FE, Kübel C, Richards R (2006) Chem Eur 12:2343
18. Pawelec B, Venezia AM, La Parola V, Thomas S, Fierro JLG (2005) Appl Catal A Gen 283:165
19. Molenbroek AM, Nørskov JK (2001) J Phys Chem B 105:5450
20. Triantafyllopoulos NC, Neophytides SG (2006) J Catal 239:187
21. Chin Y-H, King DL, Roh H-S, Wang Y, Heald SM (2006) J Catal 244:153
22. Yuan G, Louis C, Delannoy L, Keane MA (2007) J Catal 247:256
23. Reichert H, Schöps A, Ramsteiner IB, Bugaev VN, Shchyglo O, Udyansky A, Dosch H, Asta M, Drautz R, Honkimäki V (2005) Phys Rev Lett 95:235703
24. Cárdenas-Lizana F, Gómez-Quero S, Keane MA (2008) Appl Catal A Gen 334:199
25. Togasaki N, Okinaka Y, Homma T, Osaka T (2005) Electrochimica Acta 51:882
26. Tavoularis G, Keane MA (1999) J Chem Technol Biotechnol 74:60
27. Guzman J, Gates BC (2003) J Phys Chem B 107:2242
28. Bus E, Prins R, van Bokhoven JA (2007) Phys Chem Chem Phys 9:3312
29. Gluhoi AC, Bogdanchikova N, Nieuwenhuys BE (2005) J Catal 232:96
30. Bond GC, Louis C, Thompson DT (2006) Catalysis by gold. Imperial College Press, London
31. Zhao F, Fujita S-I, Sun J, Ikushima Y, Arai M (2004) Catal Today 98:523
32. Khilnani VL, Chandalia SB (2001) Org Process Res Dev 5:263
33. Zhao S, Liang H, Zhou Y (2007) Catal Commun 8:1305
34. Barbier J (1997) Handbook of heterogeneous catalysis. Redox methods for preparation of bimetallic catalysts. VCH Verlagsgesellschaft mbH, Weinheim (Germany)
35. Li Z, Deng Y, Wu Y, Shen B, Hu W (2007) J Mater Sci 42:9234
36. Mulvaney P (1996) Langmuir 12:788
37. Pawelec B, Venezia AM, La Parola V, Cano-Serrano E, Campos-Martin JM, Fierro JLG (2005) Appl Surf Sci 242:380
38. Vasil'kov AYu, Nikolaev SA, Smirnov VV, Naumkin AV, Volkova IO, Podshibikhina VL (2007) Mendeleev Commun 17:268
39. Papoutsis A, Kokkinidis G (1994) J Electroanal Chem 371:231
40. Bailie JE, Abdullah HA, Anderson JA, Rochester CH, Richardson NV, Hodge N, Zhang JG, Burrows A, Kiely CJ, Hutchings GJ (2001) Phys Chem Chem Phys 3:4113
41. Claus P, Brückner A, Mohr C, Hofmeister H (2000) J Am Chem Soc 122:11430